

OPEN ACCESS

Pourbaix Diagrams as a Simple Route to First Principles Corrosion Simulation

To cite this article: S. C. Perry *et al* 2019 *J. Electrochem. Soc.* **166** C3186

View the [article online](#) for updates and enhancements.

You may also like

- [Electrochemical Response of Ferroelectric PbZr_{0.52}Ti_{0.48}O₃ Thin Films](#)
Leo Small, Christopher Appleby, Jon F. Ihlefeld *et al.*
- [Pourbaix Diagrams As a Root for the Simulation of Polarization Curves for Corroding Metal Surfaces](#)
Samuel C Perry and Janine Mauzeroll
- [Electrochemical phase diagrams of Ni from *ab initio* simulations: role of exchange interactions on accuracy](#)
Liang-Feng Huang and James M Rondinelli

Your Lab in a Box!

The PAT-Tester-i-16: All you need for Battery Material Testing.

- ✓ **All-in-One Solution with Integrated Temperature Chamber (10-80°C)!**
No additional devices are required to measure at a stable ambient temperature.
- ✓ **Fully featured Multichannel Potentiostat / Galvanostat / EIS!**
Up to sixteen independent battery test channels, no multiplexing.
- ✓ **Ideally suited for High-Precision Coulometry!**
Measure with excellent accuracy and signal-to-noise ratio at the same time.
- ✓ **Small Footprint, Easy to Setup and Operate!**
Cableless connection of 3-electrode battery test cells. Full multi-user, multi-device control via LAN.



EL-CELL[®]
electrochemical test equipment

Learn more on our product website:



Download the Data Sheet (PDF):



Or contact us directly:

+49 40 79012-734

sales@el-cell.com

www.el-cell.com



Pourbaix Diagrams as a Simple Route to First Principles Corrosion Simulation

S. C. Perry,^{1,*} S. M. Gateman,^{1,*} L. I. Stephens,^{1,*} R. Lacasse,² R. Schulz,² and J. Mauzeroll^{1,**,z}

¹Laboratory for Electrochemical Reactive Imaging and Detection of Biological Systems, McGill University, Montreal, QC H3A 0B8, Canada

²Institut de recherche d'Hydro-Quebec, Varennes J3X 1S1, Canada

Simulation of corrosion reactions has become an important tool in the analysis of novel materials for corrosion resistant materials and applications. A number of analytical, boundary element and finite element methods currently exist in the literature, which use experimental corrosion parameters as model inputs for the extraction of simulated polarization curves, oxide growth rates, and other corrosion behaviors. Here, we propose the combination of finite element simulation with thermodynamic data from Pourbaix diagrams to allow for the simulation of metal corrosion, where individual corrosion reactions can be monitored at the metal surface.

© The Author(s) 2019. Published by ECS. This is an open access article distributed under the terms of the Creative Commons Attribution Non-Commercial No Derivatives 4.0 License (CC BY-NC-ND, <http://creativecommons.org/licenses/by-nc-nd/4.0/>), which permits non-commercial reuse, distribution, and reproduction in any medium, provided the original work is not changed in any way and is properly cited. For permission for commercial reuse, please email: oa@electrochem.org. [DOI: 10.1149/2.011191jes]



Manuscript submitted January 21, 2019; revised manuscript received March 27, 2019. Published May 2, 2019. *This paper is part of the JES Focus Issue on Advanced Techniques in Corrosion Science in Memory of Hugh Isaacs.*

In recent years simulation analysis has become commonplace in corrosion literature. Novel analytical and numerical expressions have been developed to describe uniform corrosion,¹⁻⁵ as well as localized corrosion events such as pitting,⁶⁻¹² crevice¹³⁻¹⁶ or galvanic corrosion.¹⁷⁻²¹ The use of an analytical solution is often preferable due to the significant reduction in computational cost. However the strict symmetry requirements in terms of surface reactivity and solution composition make these unsuitable for highly heterogeneous systems, such as metals with varying crystallographic orientations, composition, impurities or surface inclusions, which have significant effects on corrosion behaviors.²² Additionally, finding an analytical solution requires making a number of assumptions to simplify the analyzed system, including the use of one dimensional geometries, uniform surface reactivity, and negating the impact of solution species on the rate of reaction.¹⁸ This severely limits the scope of applicable systems.

Numerical models can function either as model-first or experiment-first, depending on whether the model starts with theoretical parameters to predict experimental behavior, or uses simulation to rationalize experimental observations. In virtually all cases across currently available models, input parameters take the form of physical parameters, such as species concentration and diffusion coefficient, and experimental parameters, such as Tafel slope (β) corrosion potential (E_{corr}) and corrosion current (j_{corr}). Values for β , E_{corr} and j_{corr} invariably come from experimental sources, whether from independent experimentation or sourced from the literature, and so there is currently an inherent requirement for electrochemical experimentation to be performed on a material before its corrosion can be simulated. This can be challenging, as determining accurate values for β , E_{corr} and j_{corr} is far from trivial; the extraction of these from potentiodynamic polarization curves (PDPs) requires the extrapolation of linear regions of the anodic and cathodic regions of the PDP, and real experimental examples often deviate from ideal linear behavior.

To combat this, a number of works have proposed rigid potential ranges for the linear fit,^{23,24} although this is not a complete solution as many metals exhibit linear regions in very different regions of their PDP due to their distinct corrosion behavior,⁵ which has led to different papers using a number of different fitting techniques to analyze the same type of data.²⁴⁻³¹ Such variance in the experimental analysis

presents a great challenge for the construction of simulations, as uncertainty around the input parameters makes it difficult to accurately validate the model output.

Here, we propose the use of thermodynamic material data from Pourbaix diagrams as the input for finite element method (FEM) simulations of metal corrosion. Rates of corrosion are determined by explicitly simulating all possible electrochemical reactions occurring between the metal surface and the surrounding environment, following Butler-Volmer kinetics. By taking rate constants from metal oxide thermal decomposition data, we are able to produce an accurate simulated PDP. Additionally, by simulating each reaction independently, we are able to model individual corrosion reactions at the metal surface, rather than working in terms of an all-encompassing corrosion potential or corrosion rate. This enables the model to determine which species will be formed during metal corrosion based on the thermodynamic data and reaction environment, rather than having the species formed being an input parameter into the model.

Experimental

Standardized polishing procedure.—Iron metal samples (99.98%) were received from Goodfellow. All specimens were sectioned into 2 cm × 2 cm samples using an abrasive cutter (abasiMet 250, Buehler, USA). Samples were fixed in cold mounting epoxy (Epofix from Struers, Canada). The substrate was abraded using a series of SiC papers (800, 1200 and 4000 grit, Struers) followed by polishing with 0.05 μm aluminum oxide suspension and a MD Chem cloth (Struers, Canada) to obtain a mirrored finish. All polishing was done using a TegraPol-25 polishing wheel and an automated TegraForce-5 polishing arm (Struers, USA). All samples were sonicated in anhydrous ethanol for 2 min to remove any alumina residue, and then dried under air.

Polarization curves.—To minimize solution resistance and provide a significantly corrosive environment, 3.5 wt% sodium chloride electrolyte was chosen as the main test solution for electrochemical measurements and corresponding simulations. Electrolytes were made using sodium chloride (99%, Sigma-Aldrich). In order to produce solutions with specific pH values, the electrolyte was titrated with either hydrochloric acid (38%, ACP) or sodium hydroxide (98%, ACP) in the presence of universal indicator (Fluka). All solutions were made using deionized water from a Milli-Q water purification system (18.2 MΩ cm resistivity). A Faraday cage and a vibration isolation

*Electrochemical Society Student Member.

**Electrochemical Society Member.

^zE-mail: janine.mauzeroll@mcgill.ca

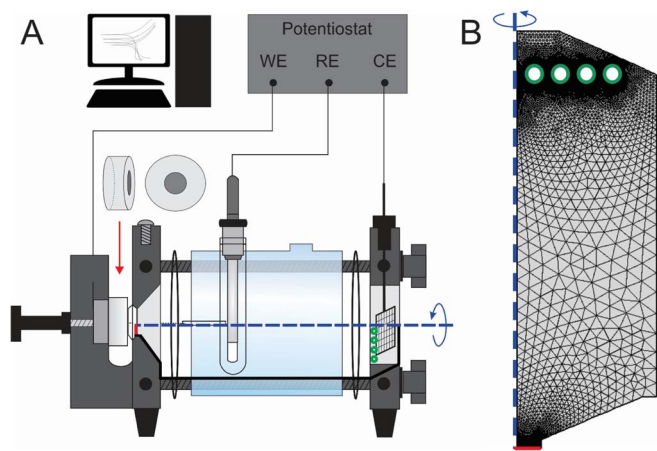


Figure 1. A: Schematic of the corrosion cell used for recorded all polarization curves. The metal sample (grey disc) is sealed in an epoxy pick and loaded into the corrosion cell (red arrow), where a 1 cm² area is exposed via an O-ring. The RE and CE are loaded into set positions, and a luggin capillary is used to bring the RE close to the WE to minimize iR drop. B: Simulated cell geometry, showing WE (red) CE (green) and rotational symmetry (blue). These areas are also overlaid in Fig 1A to show the corresponding regions in the experimental cell. WE radius = 0.564 cm to give 1 cm² area with rotational symmetry. CE is given as a series of rings to approximate the large surface area of a platinum mesh. Cell wall sizes and the angle of the lower boundary were all selected to match the experimental cell geometry. Mesh density was chosen by increasing mesh density until no change in simulated PDPs was seen.

table were used during all PDP measurements. All polarization tests were repeated at least three times to ensure reproducibility.

All PDP measurements were performed using a multi-channel VSP-300 potentiostat (BioLogic Science Instruments, USA). Experimental parameters were based on the ASTM standard test method for conducting polarization measurements on Fe-based alloys in aqueous environments.³² The cell was assembled in a three-electrode setup, with the metal sample working electrode, saturated calomel electrode (SCE) reference electrode (ATS Scientific) placed in a luggin capillary, and platinum mesh counter electrode. A bench top corrosion cell (K0235 Flat Cell, Princeton Applied Research, AMETEK Scientific Instruments) was used as the main corrosion cell for all experiments (Figure 1A). The metal sample was first immersed in the working solution for one hour in order to determine E_{corr} , before being biased ~ 300 mV more negative than the E_{corr} and then ramped positively at 0.167 mV/s until a current density limit of ~ 0.5 mA/cm² was reached. The exposed surface area of the test material was kept constant by using a 1 cm² Teflon ring to isolate a standard geometric area.

Results

Building the model.—Geometry.—All considerations for the simulation geometry were made in order to provide a simulated environment that resembles a real corrosion cell as closely as possible. Real corroding metal surfaces are highly heterogeneous, with oxidation processes being highly dependent on crystal orientation, scratches or defects, and other surface features, particularly when more extreme corrosion conditions lead to the onset of pitting or crevice corrosion, which cause significant changes to the sample topography. In all laboratory corrosion experiments, great care is taken to polish the metal surface until smooth, in order to provide as even a metal surface as possible prior to PDP recording. The corrosion cell used in this work is displayed in Figure 1A. A 1 cm² area of the working electrode is exposed to solution via an O-ring. All simulations were performed using the COMSOL 5.3 Multiphysics finite element simulation package. The simulation geometry was built according to this exposed surface area, taking into account the 1 cm² active area, the curved geometry of the cell and the volume of solution within the cell. Rather than

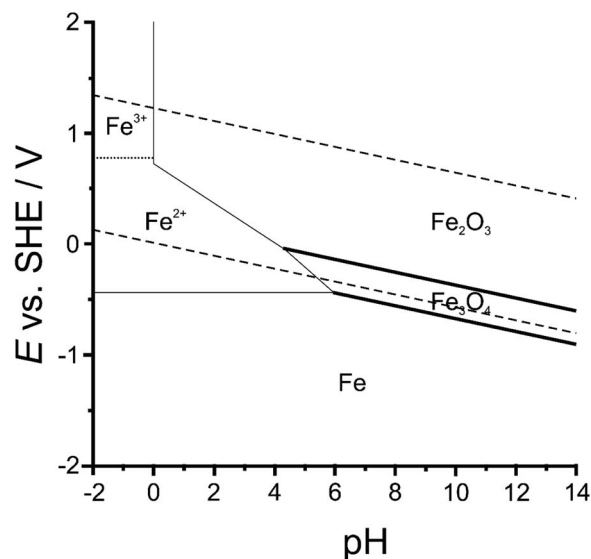


Figure 2. Replicated Pourbaix diagram for the iron-water system, $\alpha_{\text{Fe}^{2+}}|_{t=0} = 10^{-6}$ M. Bold solid lines show boundaries between two solid species, thin solid lines show boundaries between one solid and one aqueous species and dotted lines show boundaries between two aqueous species. The two dashed lines show the boundaries for the oxidation and reduction of water. Figure constructed using data from Reference 33.

using an existing boundary, the counter electrode was modelled as a series of concentric rings within the geometry to ensure that its area was significantly larger than the working area, as is the experimental case when using a platinum mesh. This also allowed the counter to be positioned at the same distance from the working electrode in both the simulation and the model. The real 3D geometry has been simplified to its 2D axisymmetric equivalent (Figure 1B), taking advantage of the plane of rotational symmetry seen through the center of the metal sample.

Construction of the model.—Most existing corrosion models are built upon experimental corrosion parameters such as E_{corr} , j_{corr} and β , which are determined using PDP analysis of the real samples. Recording polarization curves can be challenging for metals that readily corrode, as corrosion begins on immersion in solution or even immediately after polishing, which provides inherent uncertainty in the extracted corrosion parameters. Here, we propose a simulation built upon easily accessible thermodynamic parameters, as extracted from Pourbaix diagrams. This has the advantage that simulation analysis can be conducted in the absence of preceding experimental analysis, allowing the simulation to act as a means of predictive analysis. The Pourbaix diagram for the iron water system (Figure 2) shows the most thermodynamically stable species occurring at various potentials and pH, when the system is under equilibrium.

The Pourbaix diagram shows Fe, Fe₃O₄, Fe₂O₃, Fe²⁺ and Fe³⁺ as the predominant species during any aqueous PDP experiment. However, FeO, whilst not the most stable, may be an important rate determining intermediate, and so will also be simulated. It is worth noting that, at higher pH values, additional anionic corrosion products may be present. Since this work focuses on neutral to acidic environments it is not necessary to model these species currently, although this could easily be incorporated into future models. The simulation will independently look at the reactions possible between all of these species and, by running them concurrently, use the relative rates of reactions to predict which species will be present during a PDP current, and use the rate of this oxidation to extract a simulated anodic current. This method will result in some simulated reaction rates being negligibly small, where they could be excluded altogether, such as in strongly acidic electrolytes where the simulations of solid electrolytes could be omitted without significantly impacting the output. This has been done

intentionally so that the same model can be used regardless of the reaction environment, and so the model can determine which species shall be formed, rather than this being a user input. The cathodic current is assumed to come from the oxygen reduction reaction (ORR).⁵ Fluxes of all species were calculated assuming mass transport by both diffusion and convection mechanisms, assuming that the initial convective flux is zero.

$$\mathbf{N}_i = -D_i \nabla c_i + \mathbf{u} c_i \quad [1]$$

where \mathbf{N}_i is the molar flux of species ' i ', $-D_i \nabla c_i$ is the diffusive term and $\mathbf{u} c_i$ is the convection term; D_i and c_i are the diffusion coefficient and concentration of species ' i ' respectively, and \mathbf{u} is the fluid velocity. Migration is not considered due to the presence of excess electrolyte in most practical experimental set ups. The net transport at the symmetry boundaries and the cell walls was set at zero

$$\mathbf{n} \cdot \mathbf{N}_i = 0 \quad [2]$$

where \mathbf{n} is the normal unit vector, which prevents any solution species interacting with or passing through the specified boundary. To aid in simulation convergence, the concentrations of species in solution at boundaries sufficiently far from the WE were fixed at initial values

$$c_i = c_{0,i} \quad [3]$$

where $c_{0,i}$ is the concentration of species ' i ' at time $t = 0$. The working electrode boundary was defined as the only boundary with a non-zero flux

$$\mathbf{n} \cdot \mathbf{N}_i = N_{0,i} \quad [4]$$

where $N_{0,i}$ is the flux expression as defined from the difference between the rate of oxidation and reduction at the electrode surface. For all solid–solid oxide reactions, reaction rates are determined by Butler-Volmer kinetics,

$$j_{\text{ox}} = k_{\text{ox}} \cdot \exp \left\{ \frac{(1-\alpha)nF\eta}{RT} \right\} [\text{Fe}] \quad [5]$$

$$j_{\text{red}} = k_{\text{red}} \cdot \exp \left\{ \frac{-\alpha nF\eta}{RT} \right\} [\text{FeOx}] \quad [6]$$

where j_{ox} and j_{red} are the rates of oxidation and reduction, k_{ox} and k_{red} are the oxidation and reduction rate constants, α is the transfer coefficient, n is the number of electrons transferred, F is Faraday's constant, η is the applied overpotential, R is the ideal gas constant and T is the temperature. The concentration of Fe is taken as the number of Fe atoms found in a square centimeter of a Fe, which was taken as the molar volume of Fe, divided by the unit cell length. Values for k_{ox} and k_{red} come from the Arrhenius equation, where

$$k_{\text{ox}} = A \cdot \exp \left\{ \frac{-\Delta E_{a,\text{ox}}}{RT} \right\} \cdot \exp \left\{ \frac{-\gamma_{\text{ox}} L_{\text{ox}}(t)}{RT} \right\} \quad [7]$$

$$k_{\text{red}} = A \cdot \exp \left\{ \frac{-\Delta E_{a,\text{red}}}{RT} \right\} \cdot \exp \left\{ \frac{-\gamma_{\text{ox}} L_{\text{ox}}(t)}{RT} \right\} \quad [8]$$

This expression is made up of two exponential terms. The first, where A is the pre-exponential factor and ΔE_a is the activation energy, gives the initial value of k_{ox} according to the activation energy for the oxidation reaction, assuming no product is present. Activation energies for reduction reactions were approximated from isothermal kinetic studies of iron oxide reduction under hydrogen atmospheres.^{34–37} Although real activation energies in the aqueous phase are expected to differ from those determined experimentally from those recorded in the gas phase, these values provided a starting point for further refinement, where the relative magnitudes of the rate of reduction reactions between various oxides is known. For oxidation reactions, activation energies were approximated by the difference between the reduction activation energy and the enthalpy of formation for the species involved, as given by Equations 9.

$$\Delta E_{a,\text{ox}} = \Delta E_{a,\text{red}} + \Delta H_{f,\text{ox}} - \Delta H_{f,\text{red}} \quad [9]$$

The second exponential term in Equations 7 and 8 takes into account the fact that, as an oxide layer starts to form, the activation energy for further oxidation will progressively increase. Here, γ_{ox} is an activation energy gradient⁴ and $L_{\text{ox}}(t)$ is the oxide thickness at time ' t ', so as the existing oxide layer thickens the second exponential term will decrease, reducing k_{ox} and slowing the rate of further oxidation. The overpotential term (η) is defined by

$$\eta = E - E^0 - \Delta V_{\text{ox}}(t) \quad [10]$$

where E is the applied potential, E^0 is the standard redox potential for the reaction in question, and $\Delta V_{\text{ox}}(t)$ is a potential drop term. $\Delta V_{\text{ox}}(t)$ is necessary, as the oxide layer formed at the metal/solution interface is a more resistive material, and so a potential gradient will exist between the potential applied at the metal WE and the potential at the oxide solution interface. $\Delta V_{\text{ox}}(t)$ is therefore also dependent on $L_{\text{ox}}(t)$ as defined by

$$\Delta V_{\text{ox}}(t) = \epsilon_{\text{ox}} L_{\text{ox}}(t) \quad [11]$$

where ϵ_{ox} is a measure of potential drop per unit distance. This means that as the oxide layer thickens the overpotential will be decreased, hindering the formation of further oxide. It is worth noting that not all oxides are uniformly resistive at the electrode surface. Electrochemically formed oxides may form porous structures, which are less passivating than homogeneous films of the same material. Values of ϵ_{ox} used in this model take this into account, where a larger ϵ_{ox} reflects both a more resistive material and a less porous structure.

In this way, by monitoring $L_{\text{ox}}(t)$ over the course of the simulation, the model is able to constantly reduce and refine the rate of oxide formation not just based on the applied experimental conditions, but also on the state of the electrode and its surrounding environment based on the previous degree of corrosion. Values for E^0 can be simply taken from Pourbaix diagrams by using the equation of the lines between the appropriate neighboring species. In the case of species which are not shown on the Pourbaix diagram, equations for boundary lines can be calculated in the same way, so that standard potentials can be calculated for all possible reactions. In depth discussions on the procedures for deriving Pourbaix diagrams can be found in the literature.^{33,38} Briefly, for the reaction $aA + wH_2O \rightleftharpoons bB + hH^+ + ne^-$, equations of the lines come from the Nernst equation,

$$E^0 = \frac{\Delta G^0}{nF} + \log \left\{ \frac{(\alpha_B)^b (\alpha_{H^+})^h}{(\alpha_A)^a (\alpha_{H_2O})^w} \right\} \quad [12]$$

where ΔG^0 is the standard free energy change for the reaction, and α_i is the activity of species ' i '. The model uses concentration as activity with the assumption that the activity coefficient is unity. The simulated $\alpha_{\text{Fe}^{n+}}$ was from the sum of the concentration of dissolved iron from previous steps in the corrosion model and the starting concentration of dissolved iron ($\alpha_{\text{Fe}^{n+}}|_{t=0}$), which was assumed to be 10^{-6} M.

$$\alpha_{\text{Fe}^{n+}} = [\text{Fe}^{n+}] + \alpha_{\text{Fe}^{n+}}|_{t=0} \quad [13]$$

Solving this for a specific reaction, such as for $3\text{Fe}^{2+} + 4\text{H}_2\text{O} \rightleftharpoons \text{Fe}_3\text{O}_4 + 8\text{H}^+ + 2e^-$, gives the Pourbaix equation of the line.

$$E^0 = (0.98 - 0.024\text{pH} - 0.089 \log \alpha_{\text{Fe}^{2+}}) \text{ V vs. SHE} \quad [14]$$

Equation 12 shows how the standard potential for this oxidation reaction is dependent on the applied potential, the local pH, and the activity of dissolved iron in solution. By using equations such as this as the main input for the simulation, the model will be able to adjust the rate of corrosion based on the amount of iron already dissolved and based on the localized pH change that results from continued metal oxidation. Contributions to pH change from hydrolysis are not included to minimize computational costs. In the case of species existing in solution away from the WE, rates of reaction are determined from the relative concentration gradients of species involved

$$R_i = \frac{\partial c_i}{\partial t} + \nabla \cdot (-D_i \nabla c_i) + \mathbf{u} \cdot \nabla c_i = \frac{\partial c_i}{\partial t} + \nabla \mathbf{N}_i \quad [15]$$

where R_i is the reaction rate for species ' i ', $-D_i \nabla c_i$ is the diffusion term and $\mathbf{u} \cdot \nabla c_i$ is the convection term as previously defined

in Equation 1. Reaction rates are determined from the equilibrium constants (K_{eq}), which are also sourced from the Pourbaix diagram. So, for $\text{Fe}^{2+} + \text{H}_2\text{O} \rightleftharpoons \text{FeO} + 2\text{H}^+$,

$$R_{\text{Fe}^{2+}} = -R_{\text{FeO}} = k^0 \left\{ K_{\text{eq}} [\text{H}^+]^2 [\text{FeO}] - [\text{Fe}^{2+}] \right\} \quad [16]$$

where R_i is the reaction rate for species ' i ' and k^0 is a fast rate constant that keeps the system at equilibrium. The cathodic current is assumed to be solely from the reduction of oxygen at the metal surface.⁵ For simplicity, the reduction is assumed to proceed via the direct four electron reduction pathway.



The current density is then calculated from the flux of species towards the working electrode surface

$$i_{\text{sim}} = \sum_i n_i F (j_{\text{ox},i} - j_{\text{red},i}) \quad [18]$$

where i_{sim} is the simulated current density, and $j_{\text{ox},i}$ and $j_{\text{red},i}$ are the oxidative and reductive fluxes respectively for all species being simulated. A full list of all reactions studied along with rate constants used is given in the supplementary information (Table SI-1).

Modelling the counter electrode.—The function of the counter electrode (CE) is to pass the oppositely signed current with respect to the working electrode (WE) in order to maintain charge balance within the cell. In our corrosion cell, we use a platinum gauze CE. In an aerated cell, the predominant reaction at the counter electrode will be the reduction of dissolved oxygen, as defined by Equation 16, and also the reduction of water as part of the hydrogen evolution reaction (HER) according to Equation 19.



Through a combination of these reactions, net reduction or oxidation at the WE will result in water oxidation or oxygen reduction at the CE respectively. Calculating which of these reactions is dominant at any given time would require the calculation of an effective overpotential for the counter electrode that would give the correct relative fluxes of all possible reactions. As the concentration of oxygen became severely depleted, it may then be necessary to include the calculation of the exchange of oxygen gas at the liquid – air interface, which adds further computational costs. Rather than applying such a computationally expensive calculation, the model focused on the pH change at the CE, as this is likely to have the most significant impact on the overall behavior of the corrosion cell. A probe was therefore added to the model to calculate the total current being passed at any given point during the simulation. This live probe was then used to calculate the total flux of OH^- towards or away from the CE, based on whether the CE should provide a reductive or oxidative environment, respectively. Since in all proposed CE reactions the stoichiometry of OH^- and e^- are equal, the flux of OH^- can be given by

$$j_{\text{OH}, \text{CE}} = \frac{i_{\text{sim}}}{FA_{\text{CE}}} \quad [20]$$

where $j_{\text{OH}, \text{CE}}$ is the flux OH^- towards the CE, and A_{CE} is the electroactive surface area of the CE.

Comparison with experimental.—*Experimental vs. simulated PDPs.*—Explicitly simulating all aspects of the reaction environment gives this model the distinct advantage that all components of the corrosion experiment can be individually observed from the simulation data. This allows for the traditional PDP to be extracted from the model, along with concentration profiles for individual species at any given point during the potential sweep. First, the precision of the model with regards to the real corrosion cell was inspected by comparing an experimental PDP to a simulated PDP recorded under the same conditions.

Comparison of theoretical and experimental polarization curves in Figure 3 shows good agreement in all regions of the PDP, with

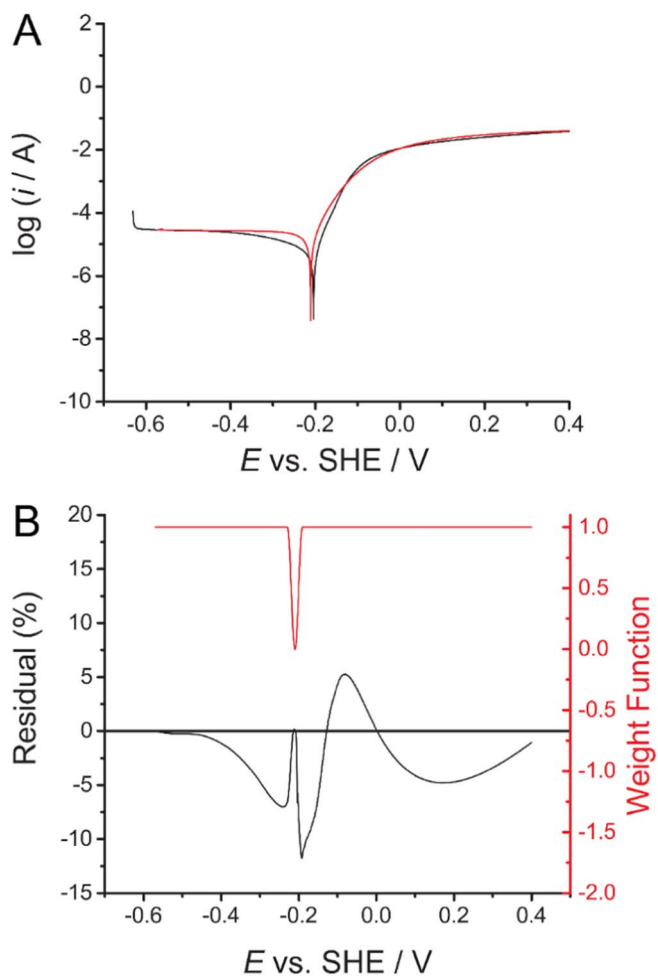


Figure 3. A: Simulated (red) and experimental (black) polarization curves for iron in 3.5% NaCl, scan rate = 0.167 mV/s, following ASTM standards.³² B: Weighting function used in percentage difference analysis (red) and percentage differences between simulated and experimental polarization curves at all potentials (black).

the average percentage difference across the whole curve being 3.3%. Figure 3B shows the calculated percentage difference across the whole graph, as well as the weighting function used in the percentage difference analysis. The merits of the weighting waveform have been discussed in previous works.⁵ Briefly, the largest changes in current are found around E_{corr} , where a small shift in E_{corr} corresponds to a massive deviation in the current, which would result in a disproportionately large percentage error. The weighting function therefore reduces the impact of the larger percentage differences about E_{corr} , without impacting the percentage difference calculated at points further than ± 10 mV from E_{corr} . Extracted values of E_{corr} from the experimental and simulated PDPs also agree within 6 mV. This is remarkably close given that no experimental electrochemical information went into the model, yet we can extract high precision electrochemical information from the simulated currents.

The anodic current density of around 10 mA cm^{-2} is characteristic of a diffusion limited response. This may seem counter intuitive as this model begins with an initial oxidation of iron to solid iron oxide products. However, since the formation of aqueous iron is thermodynamically favored, the model will simulate a rapid dissolution of the formed solid oxide to give aqueous iron, resulting in a diffusion layer containing a relatively high concentration of Fe^{2+} . High concentrations of Fe^{2+} at the electrode surface will push the dissolution equilibrium towards the solid products. At this point, the simulated rate of corrosion will become limited by the diffusion of Fe^{2+} away

from the electrode to allow for further dissolution, and therefore further corrosion. In this way, although the model initially forms a solid oxide layer, it is simulating a diffusion limited corrosion process.

Localized pH change.—During PDPs, anodic corrosion reactions at the working electrode will be balanced by the reduction of oxygen or water at the counter electrode. This results in the solution environment becoming more acidic at the working electrode due to hydrolysis, and more basic around the counter. The degree of this pH change is easy to track with the simulation through the analysis of the concentration of protons within the solution domain. However, tracking the localized change in pH during the experimental PDP proved more of a challenge. Traditional options such as the use of a glass pH probe do not offer the spatial resolution needed to track the pH gradient that is expected within the cell when moving from the working to counter electrodes. Instead, the corrosion cell was assembled as previously described with a solution containing universal indicator along with 3.5 wt % NaCl. This allowed for a continuous inspection of the pH through color changes, ranging from red at $\text{pH} < 4$ to blue at $\text{pH} > 10$. The starting pH of the solution was measured at 6 with a glass pH probe to act as a reference point for subsequent color changes.

A digital camera was fixed opposite the corrosion cell, and oriented so that it could record the contents of the entire cell, covering both the working and counter electrode environments. A video of the changing cell environment was then recorded to show the solution becoming more acidic or basic as the solution changed to red or blue respectively (available in supplementary information, accelerated 100x). In order to easily analyze the observed color changes, the video was processed in order to extract approximate values for the pH at any given point in the solution volume at any given time during the PDP. To do this, the video was first divided into 100 image frames to be individually analyzed. A script was then written in Python 2.7 to calculate mean red, green and blue (RGB) intensities for any chosen pixel in the solution volume (SI Section 5). This was done for 100 rows of pixels from the area within the corrosion cell volume, which were then averaged to give the final color change vs the corrosion cell length, starting at the left of the cell ($x = 0$, working electrode) moving towards the right of the cell $x = 6$ cm, counter electrode) (Figure SI-1). A database of RGB to pH conversion was then assembled by recording the RGB values from solutions of 3.5 wt % NaCl and universal indicator for a range of known pH, which were captured using the same digital camera in the same laboratory environment (Figure SI-3). After correcting all image frames to match the brightness level of the images used for the pH database, these recorded RGB values for each frame were cross referenced against the RGB to pH data base for all 100 frames, in order

to give a plot of pH vs. x distance for a series of time points throughout the video.

Figure 4A shows the advancement of high pH electrolyte from the counter electrode ($x = 6$ cm) towards the working electrode ($x = 0$) as the PDP proceeds. Of course, there is a degree of uncertainty to the extraction of absolute pH from RGB, such as the detection of optical artifacts in the image interfering with the RGB value, and the limited size of the RGB to pH database offering resolution to approximately the nearest 0.1 pH unit. The clear experimental change in pH around the CE revealed an interesting feature of the simulation regarding the movement of species between the CE and WE. Simulations did also show that the reactions at the CE had a greater impact on the pH change compared to the WE. However, the extent to which reactions at the CE increased the pH in bulk solution was far greater in the experimental example than was seen in the simulation (Figure 4B).

Inspection of the final section of the video (supplementary information, highlighted frames in Figure SI-2C and 2D) shows the presence of bubbles forming at the CE when the WE is being significantly oxidized. These bubbles can be seen to move away from the CE after they become significantly large. This would generate a convective flux away from the CE, and is likely a significant contributor to the asymmetrical solution front that is seen in the movement of basic species away from the CE (Figure SI-2C). While it would be possible to add a flow term from the counter electrode to the simulation to take this into account, the large degree of turbulence from this convective flow mean that a truly accurate simulation will be difficult and computationally expensive.

With or without the convective terms, the increase in pH due to the ORR or HER at the CE can be seen to substantially outweigh the decrease in pH due to the corrosion of the iron WE. This can be attributed to the incomplete hydrolysis of iron cations, which results in the total proton generation at the WE being less than the number of electrons transferred. At the CE the proton consumption is equal to the number of electrons transferred (Equation 19) and so the net pH within a closed corrosion system will be expected to increase.³⁹ The solution around the corroding iron during a PDP becomes more complex after extended polarization, as eventually the basic solution front will reach the acidic environment around the WE. This highlights in the importance of precisely modelling the corrosion cell volume, as this will impact if and when the basic solution from the CE will reach the WE surface, which has the potential to impact the recorded PDP and the observed corrosion behavior over the course of the experiment.

Oxide thickness.—Since the simulated oxide thickness, $L_{\text{ox}}(t)$, is time dependent, the rate of oxide growth over the course of the PDP can

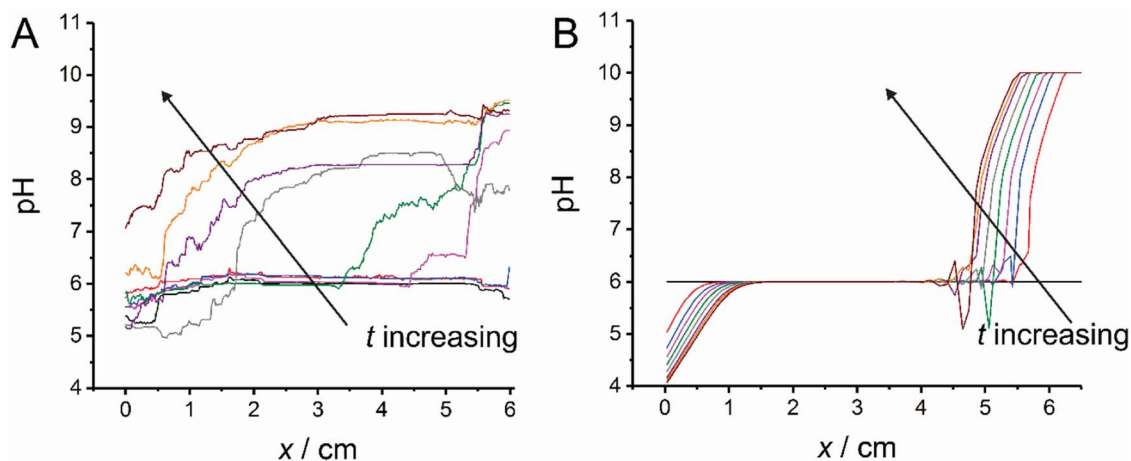


Figure 4. The pH change within the corrosion cell during a PDP. The x axis represents the length of the corrosion cell, where $x = 0$ corresponds to the WE and $x = 6$ corresponds to the CE. A shows the experimental pH change as determined from a pixel by pixel analysis of images recorded of the color change during a PDP for a corrosion cell containing universal indicator. B shows the simulated pH change during a PDP due to the consumption or formation of protons during corrosion. The simulated value was capped at pH 10 since this is the upper range of the indicator. The times elapsed correspond to 0, 63, 69, 72, 75, 78, 81, 84, 87 and 98 minutes after the start of the PDP.

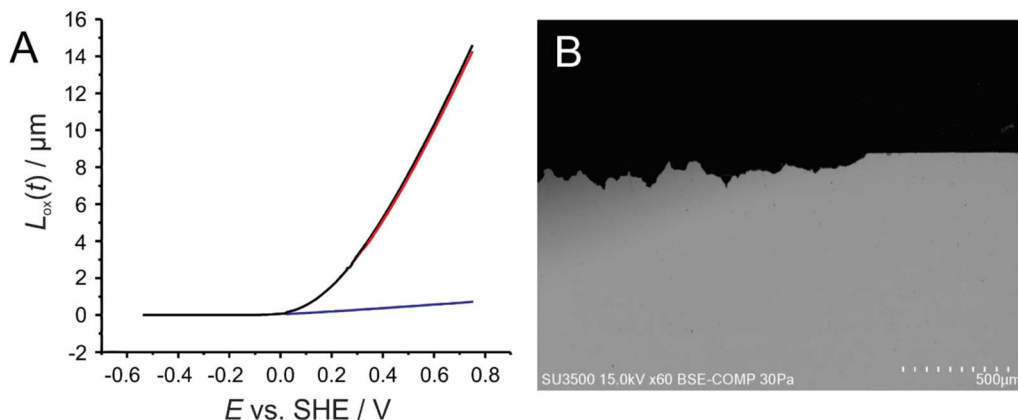


Figure 5. A) Simulated corrosion distance ($L_{\text{ox}}(t)$) at the iron surface during a PDP. The total $L_{\text{ox}}(t)$ is shown in the black curve, and the red and blue curve show contributions from iron dissolution and solid oxide formation respectively. B) SEM cross sectional image of an iron electrode after corrosion during a PDP. The grey portion is Fe metal, the black portion is empty space created during the PDP measurement and has been filled with epoxy resin.

be easily tracked. In order to compare this to experimental examples, an iron electrode was taken immediately after a PDP was recorded, dried under nitrogen flow, and then sealed in an epoxy puck. The sample was then cut in half and polished side-on to reveal a cross section of the iron oxide, with the non-corroded iron beneath. Unfortunately it was not possible to record SEM images of the oxide itself, as the oxide was too thin to observe or had poor adhesion and so did not remain attached to the sample after polarization. Instead, the total iron loss due to corrosion can be easily observed.

Since the profile of the corroded sections after polarization is highly non-uniform, an average thickness of the corroded portion was determined by calculating the area of iron lost due to corrosion, and then dividing by the sample length. The area of the iron loss was calculated using an image analysis protocol (IsoCalc ‘Get Area’ Macro,⁴⁰ CorelDraw2017). The average thickness of the corroded section was found to be 73.5 μm . Since this is a measure of iron lost to corrosion by all reactions, the experimental distance must be compared to the entirety of the simulated iron loss. The total length of simulated iron loss ($L_{\text{corr}}(t)$) was taken from the model by combining the simulated oxide thickness with the volume of iron lost to aqueous Fe^{2+}

$$L_{\text{corr}}(t) = L_{\text{FeO}}(t) + L_{\text{Fe}_3\text{O}_4}(t) + L_{\text{Fe}_2\text{O}_3}(t) + \frac{V_m \cdot \iiint \text{Fe}^{2+} dx dy dz}{A_{\text{ede}}} \quad [21]$$

where V_m is the molar volume of iron, A_{ede} is the area of the electrode, and $\iiint \text{Fe}^{2+}$ gives the total number of moles of Fe in the simulated domain. The simulated loss of iron during a PDP and the experimental cross section of the Fe electrode after polarization are shown in Figure 5.

After the simulation ran under the same conditions as the experiment, the simulated oxide loss was 14.9 μm , with most of the mass loss due formation of aqueous iron cations, rather than a solid oxide phase. The difference between the simulated and experimental values can be attributed to the fact that the simulation gives a value that treats the entire simulated surface as equal, whereas the experimental cross section represents only a small section of a heterogeneous surface. Once dissolution begins, this would reveal step, edge and similar high energy defect sites on the iron surface, which exhibit different corrosion behavior to the bulk substrate. Additionally, continual corrosion will gradually increase the surface area of the iron electrode, resulting in a greater overall corrosion rate. Together these may explain why the simulation underestimates the total depth of the iron corrosion.

Limitations of the Pourbaix diagram.—As with most approximations of complex systems there are a number of limitations to using Pourbaix diagrams to describe corroding metal systems, which have been well discussed in the literature.^{41–43} However, it is important to note that this model is built on the same equations upon which Pour-

baix diagrams are built, rather than being built from the diagrams themselves. As such, a number of the factors that limit the application of Pourbaix diagrams to experiment systems are not passed on to this model, or can be taken into account through the modification of the model.

One limitation that is particularly applicable to this model is that Pourbaix diagrams assume the system is at steady state, which is never the case for real experimental systems. By using a previously defined pre-treatment and slow sweep rate (following ASTM standards) we are able to record a PDP whilst staying reasonably close to steady state, although the dynamic nature of a PDP means that a true steady state is not really reached. The use of the ASTM standard is essential in allowing deviations from steady state in the experimental PDP to be kept to a minimum in order to make the Pourbaix diagram more applicable.

The Pourbaix diagrams also assume a homogeneously corroding surface, and so do not take into account other corroding phenomena, such as pitting or crevice corrosion. This problem is not specific to Pourbaix diagrams, but affects many finite element models, particular when a 2D simulated geometry is rotated to model a 3D reaction environment. Just as the Pourbaix diagram represents an average reaction environment at equilibrium, the 2D FEM represents an average corroding environment, which gives an average behavior of a substrate that in reality will likely be partly active and partly passivated. However, whilst the Pourbaix diagram itself assumes a homogeneously active surface, the equations used to build the model could be used to describe a heterogeneously reacting surface though FEM. For example, if a complex 3D geometry were built that included a bulk domain of iron with a thick oxide layer, where there was a scratch that revealed the bare iron surface, this model would predict a slow rate of corrosion at the bulk oxide, whilst simultaneously predicting a rapid rate of reaction at the depassivated surface.




A further limitation in the Pourbaix diagram comes with the treatment of aqueous and solid corrosion products. As well as only showing the most thermodynamically stable product, Pourbaix diagrams assume that all solid corrosion products are passivating. The top right portion of Figure 2 is often described as the ‘passivated region’, and so it might be assumed that the additional corrosion is slowed by many orders of magnitude in this region. Real experimental systems may not exhibit uniform passivity due to porosity in the passive film allowing a certain amount of access to the metal surface. This is before mentioning the added complexity in trying to predict the point at which the passive film may break down, giving a greatly enhanced rate of corrosion at the exposed surface. This model aims to encompass the effect of porosity in the film within the ϵ_{ox} parameter, where a porous oxide would be reflected in a smaller value of ϵ_{ox} . Prediction of passive film breakdown is a field in corrosion symmetry on its own and remains challenging.^{44,45}

Finally, most Pourbaix diagrams only consider the reactions of a single metal, which is not applicable to most industrial applications that require more complex metal alloys. This is a trend that is starting to change, with recent works developing Pourbaix diagrams for CrC,⁴⁶ FeCrNi⁴⁷ and NiTi⁴⁸ alloys to name a few. Calculations involved can be computationally expensive, as would be the resultant simulation given the large number of possible reaction occurring at a corroding alloy surface. Further work would be needed to determine the feasibility of this type of model towards metal alloys.

Conclusions

A finite element model has been constructed for the simulation of iron corrosion during a PDP experiment. The basis of this model comes from the Pourbaix diagram, where all possible corrosion reactions between the iron starting material and between various corrosion products are considered and explicitly simulated. The model gives a good agreement with the simulated current, and also predicts the localized pH around the counter electrode, and mass loss from the iron surface due to corrosion, where aqueous iron appears to be the dominant corrosion product. During a simulation, the state of the electrode surface is considered, where increased oxide thickness at the electrode surface results in a decreased rate of further oxidation at that specific point. This opens the possibility of expanding this model for more heterogeneous surfaces, such as a scratch in a passivated metal surface, where the model would give a greater rate of corrosion at the scratch compared to the bulk passivated surface.

ORCID

S. C. Perry  <https://orcid.org/0000-0002-6263-6114>
 L. I. Stephens  <https://orcid.org/0000-0002-0064-7555>
 J. Mauzeroll  <https://orcid.org/0000-0003-4752-7507>

References

1. R. E. Melchers, *Corros. Sci.*, **45**, 923 (2003).
2. W. Sun and S. Nešić, *Corrosion*, **65**, 291 (2009).
3. A. Kahyarian, M. Singer, and S. Nesić, *J. Nat. Gas Sci. Eng.*, **29**, 530 (2016).
4. M. Momeni and J. C. Wren, *Faraday Discuss.*, **180**, 113 (2015).
5. L. I. Stephens, S. C. Perry, S. M. Gateman, R. Lacasse, R. Schulz, and J. Mauzeroll, *J. Electrochem. Soc.*, **164**, E3576 (2017).
6. S. M. Sharland, *Corros. Sci.*, **27**, 289 (1987).
7. D. R. Gunasegaram, M. S. Venkatraman, and I. S. Cole, *Int. Mater. Rev.*, **59**, 84 (2014).
8. N. Sridhar, *Corrosion*, **73**, 18 (2016).
9. J. Srinivasan, C. Liu, and R. G. Kelly, *J. Electrochem. Soc.*, **163**, C694 (2016).
10. P. Marcus, V. Maurice, and H. H. Strehblow, *Corros. Sci.*, **50**, 2698 (2008).
11. G. T. Gaudet, W. T. Mo, T. A. Hatton, J. W. Tester, J. Tilly, H. S. Isaacs, and R. C. Newman, *AIChE J.*, **32**, 949 (1986).
12. N. J. Laycock and R. C. Newman, *Corros. Sci.*, **39**, 1771 (1997).
13. A. Keating and S. Nešić, *Corrosion*, **57**, 621 (2001).
14. F. M. Song, D. A. Jones, and D. W. Kirk, *Corrosion*, **61**, 145 (2005).
15. J. C. Walton, *Corros. Sci.*, **30**, 915 (1990).
16. J. C. Walton, G. Cragnolino, and S. K. Kalandros, *Corros. Sci.*, **38**, 1 (1996).
17. A. Stenta, S. Basco, A. Smith, C. B. Clemons, D. Golovaty, K. L. Kreider, J. Wilder, G. W. Young, and R. S. Lillard, *Corros. Sci.*, **88**, 36 (2014).
18. G.-L. Song, *Corros. Sci.*, **52**, 455 (2010).
19. A. Atrens, Z. Shi, and G. L. Song, in *Corrosion of Magnesium Alloys*, p. 455, Woodhead Publishing (2011).
20. R. S. Munn and O. F. Devereux, *Corrosion*, **47**, 618 (1991).
21. J. X. Jia, G. Song, and A. Atrens, *Corros. Sci.*, **48**, 2133 (2006).
22. S. M. Gateman, L. I. Stephens, S. C. Perry, R. Lacasse, R. Schulz, and J. Mauzeroll, *npj Mat. Deg.*, **2**, 1 (2018).
23. W. S. Tait, *An Introduction to Electrochemical Corrosion Testing for Practicing Engineers and Scientists*, PairODocs Publications (1994).
24. E. Poorqasemi, O. Abootalebi, M. Peikari, and F. Haqdar, *Corros. Sci.*, **51**, 1043 (2009).
25. G. Song, A. Atrens, and M. Dargusch, *Corros. Sci.*, **41**, 249 (1998).
26. M.-C. Zhao, P. Schmutz, S. Brunner, M. Liu, and G.-I. Song, and Atrens, A. *Corros. Sci.*, **51**, 1277 (2009).
27. Z. Shi, M. Liu, and A. Atrens, *Corros. Sci.*, **52**, 579 (2010).
28. A. J. Bard, M. Stratmann, and G. S. Frankel, *Encyclopedia of Electrochemistry, Corrosion and Oxide Films*, Wiley (2003).
29. L. Y. Xu and Y. F. Cheng, *Corros. Sci.*, **73**, 150 (2013).
30. J. Ge and O. B. Isgor, *Mater. Corros.*, **58**, 573 (2007).
31. X. L. Zhang, Z. H. Jiang, Z. P. Yao, Y. Song, and Z. D. Wu, *Corros. Sci.*, **51**, 581 (2009).
32. ASTM Standard G61-86, 2014, "Standard Test Method for Conducting Cyclic Potentiodynamic Polarization Measurements for Localized Corrosion Susceptibility of Iron-, Nickel-, or Cobalt-Based Alloys," ASTM International, West Conshohocken, PA
33. E. D. Verink, in *Uhlig's Corrosion Handbook*, p. 93, John Wiley & Sons, Inc. (2011).
34. B. Hou, H. Zhang, H. Li, and Q. Zhu, *Chin. J. Chem. Eng.*, **20**, 10 (2012).
35. H.-Y. Lin, Y.-W. Chen, and C. Li, *Thermochim. Acta*, **400**, 61 (2003).
36. I. I. J. Moon, C.-H. Rhee, and D.-J. Min, *Steel Res.*, **69**, 302 (1998).
37. K. Piotrowski, K. Mondal, H. Lorethova, L. Stonawski, T. Szymański, and T. Wiltowski, *Int. J. Hydrogen Energy*, **30**, 1543 (2005).
38. L. L. Pesterfield, J. B. Maddox, M. S. Crocker, and G. K. Schweitzer, *J. Chem. Educ.*, **89**, 891 (2012).
39. R. G. Kelly, J. R. Scully, D. Shoesmith, and R. G. Buchheit, *Electrochemical Techniques in Corrosion Science and Engineering*, Taylor & Francis (2002).
40. N. Wilkinson, *Get Area Version C*, IsoCalc (2004).
41. Z. Ahmad, in *Principles of Corrosion Engineering and Corrosion Control*, Z. Ahmad, Editor, p. 9, Butterworth-Heinemann, Oxford (2006).
42. L. L. Shreir, *Corrosion: Metal/Environment Reactions*, Elsevier Science (2013).
43. E. McCafferty, *Introduction to Corrosion Science*, Springer New York (2010).
44. G. S. Frankel and N. Sridhar, *Mater. Today*, **11**, 38 (2008).
45. G. S. Frankel, T. Li, and J. R. Scully, *J. Electrochem. Soc.*, **164**, C180 (2017).
46. V. Marimuthu, I. Dulac, and K. Kannoopatti, *J. Bio. Tribo. Corros.*, **2**, 17 (2016).
47. B. Beverskog and I. Puigdomenech, *Corrosion*, **55**, 1077 (1999).
48. R. Ding, J.-X. Shang, F.-H. Wang, and Y. Chen, *Comput. Mater. Sci.*, **143**, 431 (2018).